Dynamics of one-dimensional Kerr cavity solitons

François Leo,[1,2,*] **Lendert Gelens,**[3] **Philippe Emplit,**[1] **Marc Haelterman,**[1] **and Stéphane Coen** [4]

[1] *OPERA-photonique, Université libre de Bruxelles (U.L.B.), Bruxelles, Belgium*
[2] *Photonics Research Group, Department of Information Technology, Ghent University-IMEC, Ghent B-9000, Belgium*
[3] *Applied Physics Research Group (APHY), Vrije Universiteit Brussel, Pleinlaan 2, 1050 Brussels, Belgium. e-mail : lendert.gelens@vub.ac.be*
[4] *Department of Physics, The University of Auckland, Private Bag 92019, Auckland 1142, New Zealand*
[*] *francois.leo@intec.ugent.be*

Abstract: We present an experimental observation of an oscillating Kerr cavity soliton, i.e., a time-periodic oscillating one-dimensional temporally localized structure excited in a driven nonlinear fiber cavity with a Kerr-type nonlinearity. More generally, these oscillations result from a Hopf bifurcation of a (spatially or temporally) localized state in the generic class of driven dissipative systems close to the 1 : 1 resonance tongue. Furthermore, we theoretically analyze dynamical instabilities of the one-dimensional cavity soliton, revealing oscillations and different chaotic states in previously unexplored regions of parameter space. As cavity solitons are closely related to Kerr frequency combs, we expect these dynamical regimes to be highly relevant for the field of microresonator-based frequency combs.

OCIS codes: (190.4370) Nonlinear optics, fibers; (190.3100) Instabilities and chaos.

References

1. L. A. Lugiato, "Introduction to the feature section on cavity solitons: an overview," IEEE J. Quantum Elec. **39,** 193–196 (2003).
2. G. S. McDonald and W. J. Firth, "Spatial solitary-wave optical memory," J. Opt. Soc. Am. B **7,** 1328–1335 (1990).
3. S. Barland, J. R. Tredicce, M. Brambilla, L. A. Lugiato, S. Balle, M. Giudici, T. Maggipinto, L. Spinelli, G. Tissoni, T. Knodl, M. Miller, and R. Jäger, "Cavity solitons as pixels in semiconductor microcavities," Nature **419,** 699–702 (2002).
4. F. Leo, S. Coen, P. Kockaert, S.-P. Gorza, Ph. Emplit, and M. Haelterman, "Temporal cavity solitons in one-dimensional Kerr media as bits in an all-optical buffer," Nat. Photon. **4,** 471–476 (2010).
5. V. Odent, M. Taki, and E. Louvergneaux, "Experimental evidence of dissipative spatial solitons in an optical passive Kerr cavity," New J. Phys. **13,** 113026/1–13 (2011).
6. S. Coen, H. G. Randle, T. Sylvestre, and M. Erkintalo, "Modeling of octave-spanning Kerr frequency combs using a generalized mean-field Lugiato-Lefever model," Opt. Lett. **38,** 37–39 (2013).
7. M. C. Cross and P. C. Hohenberg, "Pattern formation outside of equilibrium," Rev. Mod. Phys. **65,** 851–1112 (1993).
8. J. Wu, R. Keolian, and I. Rudnick, "Observation of a nonpropagating hydrodynamic soliton," Phys. Rev. Lett. **52,** 1421–1424 (1984).
9. H. C. Kim, R. L. Stenzel, and A. Y. Wong, "Development of 'cavitons' and trapping of RF field," Phys. Rev. Lett. **33,** 886–889 (1974).
10. R. Richter and I. V. Barashenkov, "Two-dimensional solitons on the surface of magnetic fluids," Phys. Rev. Lett. **94,** 184503/1–4 (2005).

#185353 - $15.00 USD Received 13 Feb 2013; revised 20 Mar 2013; accepted 21 Mar 2013; published 5 Apr 2013

11. P. B. Umbanhowar, F. Melo, and H. L. Swinney, "Localized excitations in a vertically vibrated granular layer," Nature **382,** 793–796 (1996).
12. A. Ustinov, "Solitons in Josephson junctions," Physica D **123,** 315–329 (1998).
13. B. Ermentrout, X. Chen, and Z. Chen, "Transition fronts and localized structures in bistable reaction-diffusion equations," Physica D **108,** 147–167 (1997).
14. V. K. Vanag, A. M. Zhabotinsky, and I. R. Epstein, "Oscillatory clusters in the periodically illuminated, spatially extended Belousov-Zhabotinsky reaction," Phys. Rev. Lett. **86,** 552–555 (2001).
15. O. Lejeune, M. Tlidi, and P. Couteron, "Localized vegetation patches: A self-organized response to resource scarcity," Phys. Rev. E **66,** 010901 (2002).
16. B. Schäpers, M. Feldmann, T. Ackemann, and W. Lange, "Interaction of localized structures in an optical pattern-forming system," Phys. Rev. Lett. **85,** 748–751 (2000).
17. S. Barbay, X. Hachair, T. Elsass, I. Sagnes, and R. Kuszelewicz, "Homoclinic snaking in a semiconductor-based optical system," Phys. Rev. Lett. **101,** 253902 (2008).
18. O. Lioubashevski, Y. Hamiel, A. Agnon, Z. Reches, and J. Fineberg, "Oscillons and propagating solitary waves in a vertically vibrated colloidal suspension," Phys. Rev. Lett. **83,** 3190–3193 (1999).
19. C. Elphick, G. Iooss, and E. Tirapegui, "Normal form reduction for time-periodically driven differential equations," Phys. Lett. A **120,** 459–463 (1987).
20. L. A. Lugiato and R. Lefever, "Spatial dissipative structures in passive optical systems," Phys. Rev. Lett. **58,** 2209–2211 (1987).
21. K. Nozaki and N. Bekki, "Chaotic solitons in a plasma driven by an RF field," J. Phys. Soc. Jpn. **54,** 2363–2366 (1985); ibid. Physica D **21,** 381 (1986)
22. D. Turaev, A. G. Vladimirov, and S. Zelik, "Long-range interaction and synchronization of oscillating dissipative solitons," Phys. Rev. Lett. **108,** 263906/1–5 (2012).
23. A. B. Matsko, A. A. Savchenkov, and L. Maleki, "On excitation of breather solitons in an optical microresonator," Opt. Lett. **37,** 4856–4858 (2012).
24. D. Gomila, A. Scroggie, and W. Firth, "Bifurcation structure of dissipative solitons," Physica D **227,** 70–77 (2007).
25. P. Del'Haye, A. Schliesser, O. Arcizet, T. Wilken, R. Holzwarth, and T. J. Kippenberg, "Optical frequency comb generation from a monolithic microresonator," Nature **450,** 1214–1217 (2007).
26. M. A. Foster, J. S. Levy, O. Kuzucu, K. Saha, M. Lipson, and A. L. Gaeta, "Silicon-based monolithic optical frequency comb source," Opt. Express **19,** 14233–14239 (2011).
27. A. Tierno, F. Gustave, and S. Barland, "Class A mode-locked semiconductor ring laser," Opt. Lett. **37,** 2004-2006 (2012).
28. W. J. Firth, G. K. Harkness, A. Lord, J. M. McSloy, D. Gomila, and P. Colet, "Dynamical properties of two-dimensional Kerr cavity solitons," J. Opt. Soc. Am. B **19,** 747–752 (2002).
29. M. Haelterman, S. Trillo, and S. Wabnitz, "Dissipative modulation instability in a nonlinear dispersive ring cavity," Opt. Commun. **91,** 401–407 (1992).
30. A. J. Scroggie, W. J. Firth, G. S. McDonald, M. Tlidi, R. Lefever, and L. A. Lugiato, "Pattern formation in a passive Kerr cavity," Chaos, Solitons & Fractals **4,** 1323–1354 (1994).
31. G. P. Agrawal, *Nonlinear Fiber Optics*, 4th ed. (Academic Press, 2006).
32. K. Wiesenfeld, "Noisy precursors of nonlinear instabilities," J. Stat. Phys. **38,** 1071–1097 (1985).
33. I. S. Aranson and L. Kramer, "The world of the complex Ginzburg-Landau equation," Rev. Mod. Phys. **74,** 99–143 (2002).
34. O. Descalzi, C. Cartes, J. Cisternas, and H. R. Brand, "Exploding dissipative solitons: The analog of the Ruelle-Takens route for spatially localized solutions," Phys. Rev. E **83,** 056214/1–6 (2011).
35. J. M. Soto-Crespo, N. Akhmediev, and A. Ankiewicz, "Pulsating, creeping, and erupting solitons in dissipative systems," Phys. Rev. Lett. **85,** 2937–2940 (2000).
36. T. Kapitula and B. Sandstede, "Stability of bright solitary-wave solutions to perturbed nonlinear Schrödinger equations," Physica D **124,** 58–103 (1998).
37. P. Grelu and N. Akhmediev, "Dissipative solitons for mode-locked lasers," Nat. Photon. **6,** 84–92 (2012).
38. L. Gelens and E. Knobloch, "Traveling waves and defects in the complex Swift-Hohenberg equation," Phys. Rev. E **84,** 056203/1–22 (2011).
39. A. G. Vladimirov, S. V. Fedorov, N. A. Kaliteevskii, G. V. Khodova, and N. N. Rosanov, "Numerical investigation of laser localized structures," J. Opt. B: Quantum Semiclass. Opt. **1,** 101–106 (1999).
40. N. V. Alexeeva, I. V. Barashenkov, and D. E. Pelinovsky, "Dynamics of the parametrically driven NLS solitons beyond the onset of the oscillatory instability," Nonlinearity **12,** 103–140 (1999).
41. J. Burke, A. Yochelis, and E. Knobloch, "Classification of spatially localized oscillations in periodically forced dissipative systems," SIAM J. Appl. Dyn. Syst. **7,** 651–711 (2008).
42. Y.-P. Ma, J. Burke, and E. Knobloch, "Defect-mediated snaking: A new growth mechanism for localized structures," Physica D **239,** 1867–1883 (2010).
43. D. Gomila, A. Jacobo, M. A. Matías, and P. Colet, "Phase-space structure of two-dimensional excitable localized structures," Phys. Rev. E **75,** 026217/1–10 (2007).

#185353 - $15.00 USD Received 13 Feb 2013; revised 20 Mar 2013; accepted 21 Mar 2013; published 5 Apr 2013

44. C. Grebogi, E. Ott, and J. A. Yorke, "Crises, sudden changes in chaotic attractors, and transient chaos," Physica D **7,** 181–200 (1983).
45. E. M. Izhikevich, "Neural excitability, spiking and bursting," Int. J. Bifurcation Chaos **10,** 1171–1266 (2000).
46. L. Gelens, L. Mashal, S. Beri, W. Coomans, G. Van der Sande, J. Danckaert, and G. Verschaffelt, "Excitability in semiconductor microring lasers: Experimental and theoretical pulse characterization," Phys. Rev. A **82,** 063841/1–9 (2010).
47. W. Coomans, L. Gelens, S. Beri, J. Danckaert, and G. Van der Sande, "Solitary and coupled semiconductor ring lasers as optical spiking neurons," Phys. Rev. E **84,** 036209/1–8 (2011).
48. T. J. Kippenberg, R. Holzwarth, and S. A. Diddams, "Microresonator-based optical frequency combs," Science **332,** 555–559 (2011).

1. Introduction

Solitons in optical resonators, often called cavity solitons [1], have attracted a lot of interest because of their possible application as information carriers in all-optical memories [2]. Experimentally, they have first been observed in two-dimensional (2D) spatial resonators [3] and recently also in one-dimensional (1D) Kerr cavities [4, 5]. Moreover it was recently shown that they correspond to the temporal profile of microresonator-based Kerr frequency combs [6]. These solitons belong to the broad class of localized dissipative structures (LSs). LSs are common in a broad range of pattern forming systems and as such have received a lot of attention in many different fields. They exist due to the balance between nonlinearity, diffusion-like processes, dissipation, and a (homogeneous) external forcing [7]. Experimental observations have been reported in hydrodynamics [8], plasma physics [9], magnetic fluids [10], layers of sand [11], superconductivity [12], chemical reactions [13, 14], biology [15] and optics [3–5, 16, 17]. A great deal of theoretical work on dynamical instabilities of LSs in space and time has been reported too. Yet, experimental investigations of the dynamics of LSs are considerably rarer. Observations of localized time oscillations embedded in a homogeneous background, also referred to as *oscillons*, have been limited to systems driven by a spatially homogeneous periodic forcing with its frequency Ω near twice the natural oscillation frequency ω of the system [11, 18]. More generally, however, oscillons can be found in the forced complex Ginzburg-Landau equation (FCGLE) [19] modeling the dynamical behavior of the oscillation amplitude near all strong resonances of the form $\Omega : \omega = n : 1$, with $n = 1, 2, 3 \ldots$

In this paper, we consider oscillating cavity solitons (CSs) in a high finesse optical fiber resonator. The slowly-varying complex amplitude E of the electric field in such cavities is described by the well-known mean-field Lugiato-Lefever equation (LLE), which is a particular realization of the FCGLE at the $1 : 1$ resonance [20]. With a setup similar to that of [4], i.e., for a 1D system, we report the first experimental observations of periodic oscillatory behaviors of CSs. Theoretically, these have been known to occur for a long time [21] (see also [22] and references therein) and have also been recently discussed in the context of microresonators [23]. On top of our experimental results, we show through a detailed numerical analysis that, in addition to time-periodic oscillations, we also find temporal chaos, transient chaos and spatio-temporal chaos. Note that we sometimes refer here to a spatial scale instead of the fast time scale (see Section 2 below), this because of the formal equivalence with the LLE for 1D spatial systems and to avoid confusion by talking about two different time scales. All these dynamical regimes arise for higher values of the frequency detuning than previously considered [24] and, although most of these were out of reach of our experimental setup, these regions could become accessible by using other devices such as microresonators or semiconductor lasers [25–27].

In Section 2, we introduce a mean-field model for our 1D optical fiber resonator and present the relationships between the normalized and experimental parameters. In Section 3, we describe the experimental set-up and present measurements of stable and oscillating CSs. These measurements are then compared to numerical simulations of the mean-field model using the

#185353 - $15.00 USD Received 13 Feb 2013; revised 20 Mar 2013; accepted 21 Mar 2013; published 5 Apr 2013

corresponding experimental parameters in Section 4. Moreover, a numerical analysis of different dynamical instabilities of the 1D temporal CS is performed, showing time-periodic oscillations and different chaotic states. Finally in Section 5, we conclude with a short discussion.

2. Mean field model

The system under consideration is a high finesse fiber cavity, for which the evolution of the intracavity field $E(t,\tau)$ is governed by a dimensionless mean-field equation [20]

$$\frac{\partial E(t,\tau)}{\partial t} = \left[-1+\mathrm{i}(|E(t,\tau)|^2-\Delta)-\mathrm{i}\eta\frac{\partial^2}{\partial\tau^2}\right]E(t,\tau)+S, \tag{1}$$

where t is the slow time rescaled with respect to the cavity photon lifetime, τ is the fast time scale, Δ is the cavity detuning, S is the continuous driving field amplitude and η is the sign of the group-velocity dispersion coefficient of the fiber β_2. The normalization is such that

$$t \rightarrow \frac{\alpha t}{t_\mathrm{R}}, \tag{2}$$

$$\tau \rightarrow \tau\sqrt{\frac{2\alpha}{|\beta_2|L}}, \tag{3}$$

$$E \rightarrow E\sqrt{\frac{\gamma L}{\alpha}}, \tag{4}$$

$$S = E_\mathrm{in}\sqrt{\frac{\gamma L\theta}{\alpha^3}}, \tag{5}$$

where α is equal to half the total cavity losses expressed in percentage of power lost per round-trip, t_R is the cavity round-trip time, L is the cavity length, while γ is the Kerr nonlinearity coefficient. The cavity detuning is defined as $\Delta=\delta/\alpha$ with $\delta = 2m\pi-\phi_0$, where ϕ_0 is the overall cavity round-trip phase shift and m is the order of the closest cavity resonance. E_in is the amplitude of the driving field incident on the cavity input coupler with intensity transmission coefficient θ and has units such that $P_\mathrm{in}=|E_\mathrm{in}|^2$ is the driving power. The field at the cavity output, E_out, which results from the interference between the field leaving the cavity and the part of the driving beam reflected on the input coupler, can then be expressed from our dimensionless variables as

$$E_\mathrm{out} = \sqrt{\frac{\alpha\theta}{\gamma L}}\left(E-\kappa S\right), \tag{6}$$

where $\kappa=\alpha/\theta$. The cavity output power is given by $P_\mathrm{out}=|E_\mathrm{out}|^2$.

When $\Delta<\sqrt{3}$, the homogeneous steady-state solutions have a monostable response in function of the driving S [24, 28]. For higher values of the detuning, $\Delta>\sqrt{3}$, the homogeneous steady state response of (1) has the characteristic S-shape of a bistable hysteresis cycle [29]. In the case of anomalous dispersion, the upper branch of homogeneous solutions is unstable [30]. However, in a suitable range of driving powers, a stable branch of patterned solutions coexists with the stable homogeneous lower-branch solutions. This allows for the existence of CSs as a pair of bound fronts connecting both solutions. The CSs can be excited through an incoherent writing process (see [4]).

#185353 - $15.00 USD Received 13 Feb 2013; revised 20 Mar 2013; accepted 21 Mar 2013; published 5 Apr 2013

3. Experimental demonstration of cavity soliton oscillations

3.1. System set-up and cavity soliton excitation scheme

Our setup is identical to the one introduced in [4]. A simplified version is depicted in Figure 1. It mainly consists of a 90/10 fiber coupler closed on itself. The continuous-wave (CW) driving beam at 1550 nm is injected through one arm of the coupler in which it interacts coherently with the intracavity field. For this to occur, the driving laser must have a coherence length much longer than the fiber cavity. We use a DFB laser with a 1 kHz bandwidth. The cavity is 380 m long and contains a piezo-electric stretcher connected to a PID controller for an active stabilization of the fiber length (the error signal is derived from the cavity output power itself, i.e., from the power reflected off the cavity), and a 60 dB isolator to suppress stimulated Brillouin scattering [31]. The total round-trip losses are 26% ($\alpha = 0.13$), corresponding to a relatively high finesse of 24 and to 22-kHz-wide resonances. The largest values of normalized driving power and detuning reached in the experiment were, respectively, $|S|^2 = 8.5$ and $\Delta = 4.1$, corresponding to a CW driving power of $P_{\text{in}} = 274$ mW and a phase detuning $\delta = 0.5$ rad. Incoherent excitation of a CS is performed with a single 4 ps-wide writing pulse generated by a 10 MHz mode-locked laser at 1535 nm. It is launched into the cavity through the input couler and removed by a wavelength-division multiplexer (WDM) coupler after 90 m to avoid the excitation of a second CS as the 1535 nm wave travels at a different group velocity than the intra-cavity field. Note that the maximum detuning we could achieve was constrained both by the necessity to stay around the resonance, for the error signal of the PID controller to have a significant slope, and by the limited power of the writing pulses.

Due to the π phase-shift difference that exists between the two ports of the fiber coupler [see the minus sign in Eq. (6), necessary to satisfy energy conservation], the CSs appear as inverted peaks on a strong CW background at the output port. In our single-shot detection system, which has a bandwidth limited to 1 GHz, these inverted peaks, which are typically a few picoseconds in duration, are so severely broadened that they are in practice completely smeared out in the background and invisible on the oscilloscope. To circumvent this problem, we used a sequence of two identical narrow optical bandpass filters in front of the photodiode. These filters are dense WDM fiber couplers centered at 1552 nm, slightly above the wavelength

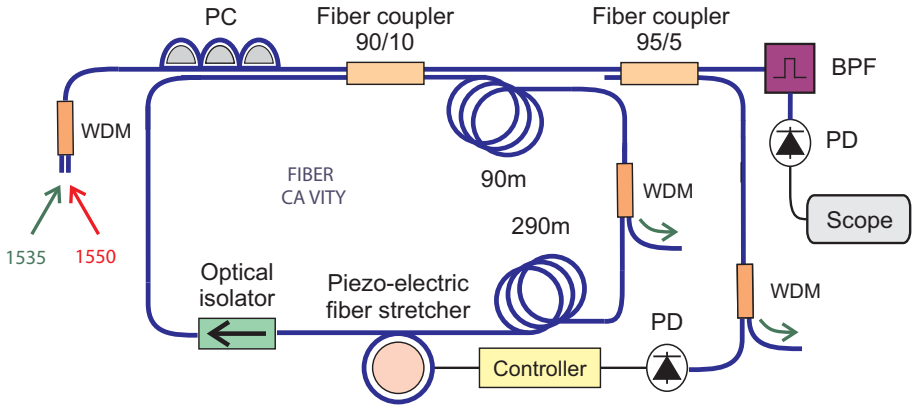

Figure 1. Experimental setup: Our cavity is made up of 380 m of standard single mode fiber. The driving and addressing beams are combined through a wavelength division multiplexer (WDM). Part of the output beam is used to actively stabilize the cavity lenth, while the rest is directed towards an oscilloscope. PC: Polarization controller. PD: Photodiode. BPF: Optical band pass filter

#185353 - $15.00 USD Received 13 Feb 2013; revised 20 Mar 2013; accepted 21 Mar 2013; published 5 Apr 2013

of the CW driving beam, with a spectral width of 0.9 nm at 0.5 dB. This effectively removes the CW background and transforms the CSs into 10 ps bright peaks that can be detected with our 1 GHz measurement system.

3.2. Experimental results

For the different values of driving power and detuning considered, we start all our measurements by setting up the cavity in the lower-state of the homogeneous bistable response. The driving power and detuning are then held steady and, after exciting a single CS in the cavity,

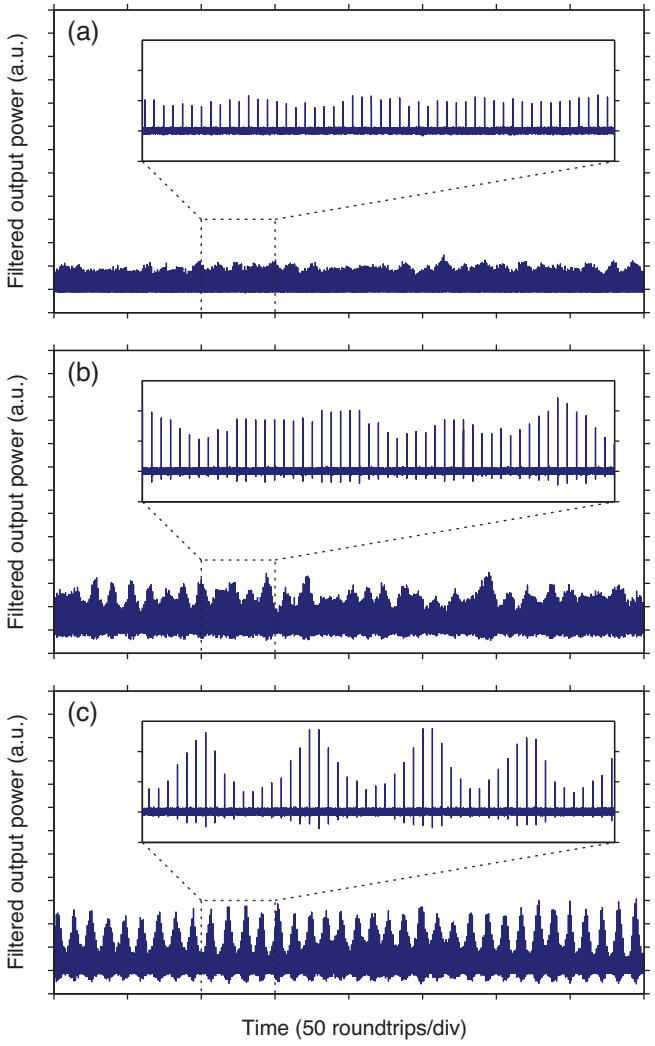

Figure 2. Oscilloscope traces (linear scaling) at the output of the cavity a few milliseconds after launching the writing pulse. The delay between subsequent pulses in the output sequences is equal to the 1.85 μs cavity round-trip time. (a) $P_{\text{in}} = 200$ mW and $P_{\text{out}} = 184$ mW, corresponding to $|S|^2 = 6.2$ and $\Delta = 3.8$. (b) $P_{\text{in}} = 236$ mW and $P_{\text{out}} = 219$ mW, corresponding to $|S|^2 = 7.3$ and $\Delta = 4.1$. (c) $P_{\text{in}} = 274$ mW and $P_{\text{out}} = 254$ mW, corresponding to $|S|^2 = 8.5$ and $\Delta = 4.1$.

#185353 - $15.00 USD Received 13 Feb 2013; revised 20 Mar 2013; accepted 21 Mar 2013; published 5 Apr 2013

we record experimental output time series (see Figure 2). From this procedure, it is clear that all the dynamical solutions shown in Figure 2 coexist with the stable homogeneous solution we started from.

Figure 2(a) shows the time evolution of a CS excited below the theoretical Hopf (i.e., oscillatory) threshold, where the CSs are expected to be stable. Here, the normalized driving power and detuning are the same as those used for the autocorrelation and spectral measurements reported in [4]. Those measurements confirmed that the pulses circulating in the cavity have a 4 ps duration and that their spectral and temporal characteristics match very well with the theoretical CS of Eq. (1). However, an ideal stable CS should keep its amplitude rigorously constant over successive roundtrips. In contrast, the measurement reported in Figure 2(a) clearly reveals the presence of pulse power fluctuations. These fluctuations are mainly caused by two factors: the amplified spontaneous emission (ASE) noise of the driving laser amplifier reaching the photodiode placed in front of the oscilloscope (we have checked that a larger level of ASE correlates with much stronger observed pulse-to-pulse variability) and — on a slower timescale — the relaxation oscillations of the driving laser [4].

Figure 2(b) shows the output time series of a CS for a driving power and detuning very close to the Hopf threshold, as theoretically predicted in the next Section. Instead of exhibiting an oscillatory behavior, the CS amplitude shows irregular changes which seem to be very sensitive to driving laser fluctuations. This behavior is expected. On the one hand, just below the oscillatory instability, one can observe a noisy precursor of the limit-cycle attractor that is to be created [32]. On the other hand, just above the Hopf instability, the system converges only very slowly to the stable limit cycle, hence is very sensitive to noisy fluctuations. When increasing the driving power further, the basin of attraction of the limit cycle becomes deeper, such that the system quickly contracts to this oscillatory attractor, even in the presence of noise. This is the situation reported in Figure 2(c), which shows the output time series of a CS excited well above the theoretical Hopf threshold. In this case, the evolution of the intracavity peak power clearly shows that the CS is in an oscillatory regime. The observed regime is characterized by a period of 11.2 roundtrips and a 70 % modulation depth.

4. Dynamical instabilities of one-dimensional cavity solitons

4.1. Oscillatory behavior of the 1D cavity soliton

Results obtained through numerical simulations of Eq. (1) for the same parameters as those used in the experiment in Figure 2 are shown in Figure 3. The simulations are performed using periodic boundary conditions with 1024 discretization points using a pseudospectral method. The system size $\Delta\tau = 50$ has been taken large enough so that boundary conditions do not affect the dynamics of the CS. The time-step used is $\delta t = 5 \times 10^{-4}$, much smaller than any relevant time scale of the system.

Figure 3(a) shows the theoretical bifurcation diagrams of the homogenous (bottom, black and grey curves) and CS (top, colored curves) states for the two values of the detuning used in the experiment, $\Delta = 3.8$ (lighter curves) and $\Delta = 4.1$ (darker curves), respectively. The CS curves represent the peak power of the corresponding pulse. The theoretical Hopf threshold is indicated on both set of curves and is $|S|^2_{\mathrm{Hopf}} = 7.1$ for $\Delta = 3.8$ and $|S|^2_{\mathrm{Hopf}} = 7.2$ for $\Delta = 4.1$, which is in good accordance with the experimental observations of Figure 2. Above the Hopf threshold, the CS solution becomes oscillatory (dashed-purple curve). Figures 3(b)–(d) provide more detailed numerical results for parameters corresponding to the largest driving power and detuning considered in the experiment [Fig. 2(c): $|S|^2 = 8.5$ and $\Delta = 4.1$]. Figure 3(b) shows the theoretical temporal intensity profile of the CS in the fiber cavity at a time where it reaches its maximum peak power, while Figure 3(c) depicts the time evolution of the peak power of the CS. Figure 3(d) shows the corresponding contour plot of the time evolution of the central part of the

#185353 - $15.00 USD Received 13 Feb 2013; revised 20 Mar 2013; accepted 21 Mar 2013; published 5 Apr 2013

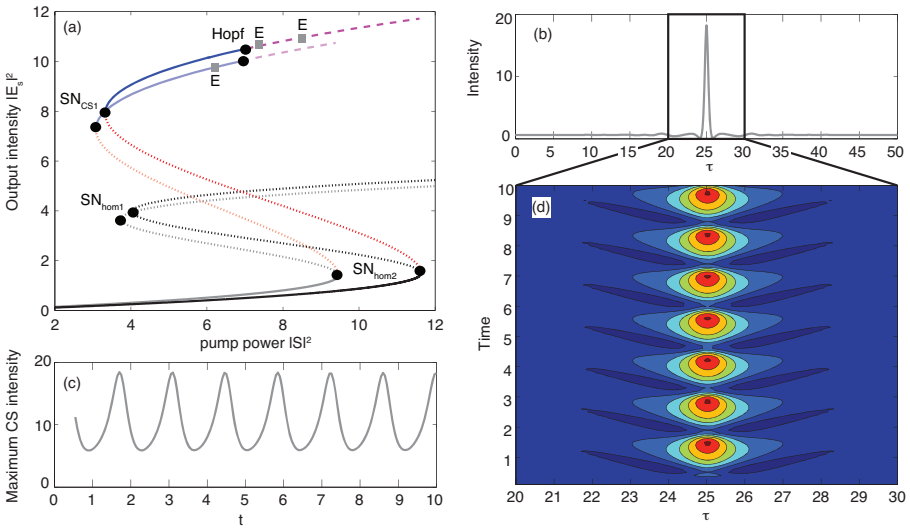

Figure 3. (a) Theoretical bifurcation diagrams corresponding to the two values of the detuning Δ used for the experimental measurements of Fig. 2. The light (dark) shades correspond to $\Delta = 3.8$ ($\Delta = 4.1$) respectively. The top curves represent the CS peak power (blue: stable CS; dotted-red: unstable saddle CS; dashed-purple: oscillatory CS), with the filled gray squares highlighting the experimental points, while the bottom S-shaped curves show the bistable behavior of the homogeneous state (where the solid (dotted) lines correspond to stable (unstable) states). (b)–(d) provide more detailed numerical results for the parameters corresponding to Fig. 2(c): $|S|^2 = 8.5$ and $\Delta = 4.1$. (b) shows the theoretical temporal intensity profile of the CS circulating inside the fiber cavity when it reaches its maximum peak power. The slow-time evolution of the CS peak power is depicted in (c). (d) shows, as a contour plot, the corresponding slow-time evolution of the temporal intensity profile of the CS.

CS profile shown in Figure 3(b). As in the experiment, time-periodic oscillations are observed. Figure 3(c) reveals a period of 1.418 in the normalized time of the LLE model. Using Eq. (3), this translates to an actual period of 10.6 roundtrips. As regards the modulation depth, let us notice that the modulation depth of the fluctuations shown in Figure 3(c) cannot be directly compared to the one of Figure 2(c) as the experimental measurements are performed behind two optical bandpass filters and after the CSs interfere with the reflected part of the driving beam. In order to compare the magnitude of the theoretical and experimental power oscillations, we calculate the profile of the CS at the output port using Eq. (6) and add a numerical filter mimicking the ones used in the experiment. This leads to a theoretical modulation depth of 95%.

Clearly the numerical results obtained from Eq. (1) compare very well with experiments, even for the rather high phase detunings used in our experiment (up to $\Delta = 4.1$, corresponding to $\delta = 0.5$ rad). Higher normalized detunings should be readily accessible experimentally by simply increasing the cavity finesse. This is not easy to achieve in fiber resonators, mainly because of the lossy intracavity isolator. However, high finesse microresonators have been recently implemented [25, 26] and should allow for studying the dynamical regimes of temporal CSs at even higher values of Δ.

Because of the near-future potential to experimentally access operating regimes with large Δ, we present in the next Section the possible dynamical instabilities of the 1D CSs of Eq. (1). The bifurcation structure and instabilities of dissipative solitons, such as e.g. pulsating, moving and

#185353 - $15.00 USD Received 13 Feb 2013; revised 20 Mar 2013; accepted 21 Mar 2013; published 5 Apr 2013

exploding solitons, have been studied in great detail in the complex Ginzburg-Landau equation [33–37], the complex Swift-Hohenberg equation [38], lasers with a saturable absorber [39], and in parametrically driven systems close to the 2:1 resonance [11, 18, 40, 41]. In contrast, soliton instabilities close to the 1:1 resonance have been studied in much less detail. In plasma physics, Nozaki and Bekki have shown theoretically that the LLE (1) can display more complicated dynamical regimes for higher values of the detuning [21]. However, such dynamical instabilities have not been observed experimentally and in optics they were never investigated for 1D CSs. Here, we study the CS behavior for $\Delta > \sqrt{3}$, thereby extending previous analysis of the LLE made for $\Delta < \sqrt{3}$ [24]. In a more general context, the bifurcation structure of localized structures in the FCGLE at the 1:1 resonance has only recently been studied [42].

4.2. Types of dynamical instabilities

Figure 4 shows the different dynamical regimes of the CS that can be observed for a value of the detuning $\Delta = 10$. The panels on the left-hand side are projections of the time-evolution of the LLE (1) onto a two-dimensional phase-space (φ, R) defined by the phase φ and the amplitude R of the center of the CS. The middle panels show the corresponding time evolution of the intensity R^2 of the center of the CS, while the panels on the right-hand side similarly show contour plots of the time evolution of the intensity $|E|^2$ of the CS temporal intensity profile. From top to bottom the driving strength S is increased from (a) $S = 6$ to (d) $S = 7.1$. As the CS originally emerges through a saddle-node bifurcation (SN_{CS1}), there exist two branches of CSs: one saddle solution S_a and one possibly stable CS. In the numerical simulations presented here, we have first used a Newton-Rhapson method to detect the saddle CS S_a. As similarly demonstrated in [43], the infinite dimensional spectrum corresponding to the saddle solution only contains two eigenvalues associated with a localized eigenmode that determines the CS dynamics. The two corresponding eigenvectors give the stable and unstable directions of the saddle, $\vec{r}_s$ and $\vec{r}_u$, respectively. As an initial condition for our numerical simulations, we use the saddle solution S_a perturbed by either $\pm 0.005 \times \vec{r}_u$ such that both directions of the (infinite-dimensional) unstable manifold of the saddle are followed.

For $S = 6$, the dashed and solid black lines in Figure 4(a) show the time evolution in the two-dimensional sub-phase-space (φ, R) for both initial conditions, in each case starting from S_a. In one case (dashed line), the system relaxes to the stable homogeneous solution H_1 (this is the state from which the experiments are started, before writing a CS; see Section 3.2), while in the other case (solid line) a stable limit cycle P_1 is the long-term attractor of the system. Increasing the driving S to 6.5, a similar simulation shows H_1 and a stable two-period limit cycle P_2 as the attractors of the system [see Figure 4(b)]. Increasing S leads to oscillations with higher periodicity, eventually leading to temporal chaos (the CS remains localized in the fast time-scale τ though). The chaotic attractor of the CS is shown in Figure 4(c). For $S = 7.1$ [Figure 4(d)], the homogeneous solution H_1 is the only remaining stable attractor of the system. However, for perturbations across the stable manifold of the saddle CS S_a, the system does not immediately relax to H_1. Perturbations across this threshold lead to a large excursion in phase-space before relaxing to H_1. This excursion corresponds to a chaotic transient where the system follows the reminiscent flow of the chaotic attractor existing for lower values of S [44]. Excitation of such large excursions in phase space when crossing a threshold is also a typical characteristic of *excitability* [45]. However, in excitable systems, the shape of the excited pulses is substantially independent of the magnitude of the perturbation, which is a feature that does not apply in the present case. We remark that the observed variability in excited pulses is not unique to this system of a coherently driven nonlinear fiber resonator. A clear variability in excited optical pulses has recently also been observed theoretically and experimentally in the context of semiconductor ring lasers [46, 47]. Finally, when increasing S further, the entire

#185353 - $15.00 USD Received 13 Feb 2013; revised 20 Mar 2013; accepted 21 Mar 2013; published 5 Apr 2013

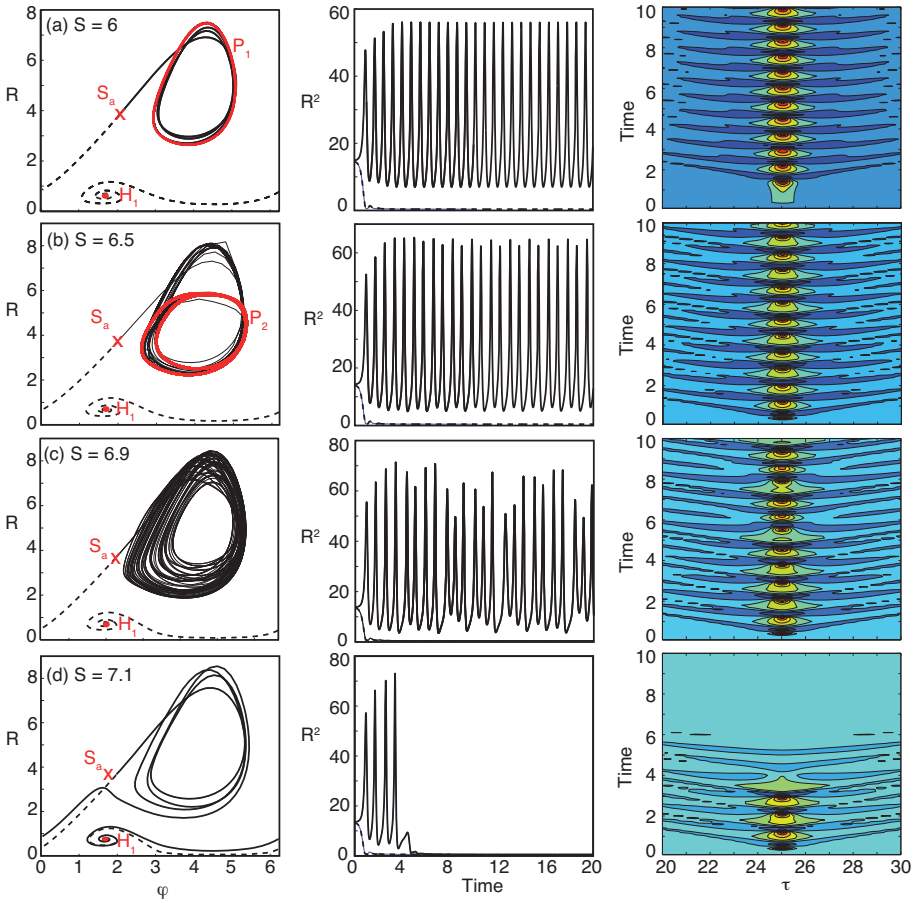

Figure 4. Panels on the left show a projection of the time-evolution of the LLE onto the 2D phase-space (φ, R) with φ and R the phase and amplitude of the center of the CS (note that the phase φ wraps at 2π). The middle panels show the corresponding time traces for the center intensity R^2. Two different initial conditions are chosen (shown in dashed and solid line): $S_a \pm 0.005 \times \vec{r}_u$. The right panels depict a contour plot showing the time evolution of the temporal intensity profile of the CS. From top to bottom the driving S is increased from 6 to 7.1, showing period-1 oscillations, period-2 oscillations, temporal chaos and transient chaos, respectively. $\Delta = 10$.

system eventually destabilizes leading not just to a localized instability, but rather to spatio-temporal chaos, see Figure 5. The white dashed line in Figure 5 shows the moment at which the system loses its perfect left-right symmetry and develops spatio-temporal chaos. The front that exists between the region with (oscillating) localized structures and the homogeneous state also loses its left-right symmetry at this point. The asymmetry in front propagation speed between the left and right side seems to be sensitive to initial conditions.

4.3. Influence of the detuning and pump power: attractor chart

Figure 6 shows an attractor chart of the LLE for detunings $\Delta > \sqrt{3}$ in the parameter space (S, Δ). For comparison, the values at which our experiments have been carried out are indicated (see legend). The saddle-node bifurcations creating the homogeneous solutions and the CS solu-

#185353 - $15.00 USD Received 13 Feb 2013; revised 20 Mar 2013; accepted 21 Mar 2013; published 5 Apr 2013

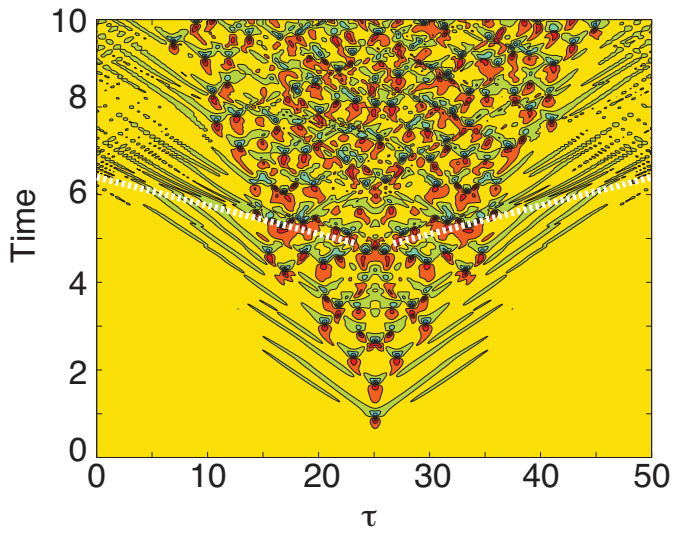

Figure 5. Contour plot showing the time evolution of a CS profile for $S = 10$, $\Delta = 10$. The white dashed line shows the moment the system loses its left-right symmetry and the system shows spatio-temporal chaos.

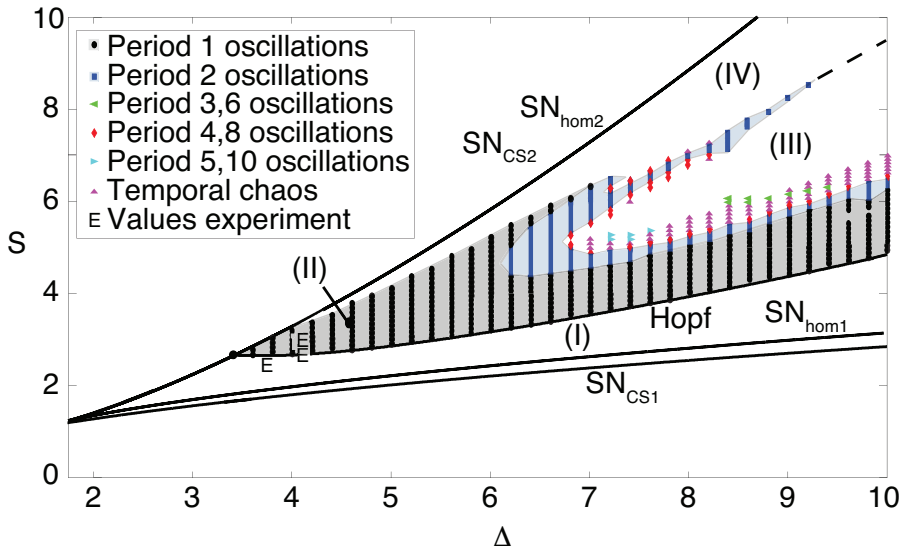

Figure 6. Different dynamical regimes of operation in the LLE for a detuning $\Delta > \sqrt{3}$.

tions are denoted by SN_{hom} and SN_{CS} [see also Figure 3(a)]. In region (I), one finds stable CSs, whereas in region (II) the CSs oscillate while retaining their localized spatial structure. There is also a wide region with oscillations with different periodicity or even temporal chaos (see legend in Figure 6). Region (III) is characterized by the transient chaos demonstrated in Figure 4(d). Finally, in region IV, the entire system destabilizes leading to spatio-temporal chaos. Such spatio-temporal chaos is already present at relatively low values of Δ, while period-2 oscillations and more complicated spatially localized temporal dynamics start at $\Delta \approx 6$. The attractor

#185353 - $15.00 USD Received 13 Feb 2013; revised 20 Mar 2013; accepted 21 Mar 2013; published 5 Apr 2013

chart has been mapped out as follows. We first used a Newton method to find the profile of the CS solution for each parameter value (the regular CS, not the saddle CS as in Figure 4). Next, we use this CS profile as initial condition to perform time evolution simulations and analyze the resulting spatio-temporal dynamics. We have verified that using different initial conditions does not noticeably change the attractor chart. Regions exhibiting multistability between attractors associated to different dynamics of a single CS cannot be excluded though. Moreover, we would like to remark that although we only consider the dynamics of single CSs here, in general such (single-peaked) CSs can coexist with other localized and extended patterns. Bifurcation diagrams related to such a highly multistable landscape are often called *snaking* diagrams. We are currently in the process of analyzing the dynamical behavior of such localized and extended patterns and its relation to the attractor chart presented here.

5. Conclusion

In conclusion, we have demonstrated experimentally and theoretically the existence of 1D localized oscillations in a high finesse fiber cavity. In the well-known Lugiato-Lefever equation describing such cavities [20], these dynamical regimes at higher values of the detuning remained hidden [24, 28, 30]. It is in this region of operation that a wealth of oscillatory behavior can be found. We have theoretically demonstrated the presence of different time-periodic oscillatory states and various chaotic states. A clear connection between the model parameters of a mean-field model for the fiber cavity and the experimental device parameters is provided. As the predicted dynamical regimes of the 1D cavity soliton are experimentally accessible by working with higher finesse optical cavities (such as, e.g., microresonators [25, 26]), we believe that this paper provides the necessary information for a future observation of the different dynamical states of the 1D cavity soliton. As such solitons are linked to so-called Kerr frequency combs [6], we foresee these dynamical regimes to have a strong impact on the field of microresonator-based Kerr frequency combs [48].

Acknowledgments

We thank D. Gomila for interesting discussions. This research was supported by the Research Foundation - Flanders (FWO) and the Belgian Science Policy Office (BelSPO) under Grant No. IAP 7-35. S. Coen also acknowledges the support of the Marsden Fund of the Royal Society of New Zealand.

#185353 - $15.00 USD Received 13 Feb 2013; revised 20 Mar 2013; accepted 21 Mar 2013; published 5 Apr 2013